JOURNAL OF THERMOPHYSICS AND HEAT TRANSFER
Vol. 20, No. 3, July–September 2006

Partial Melting and Resolidification of Metal Powder in Selective Laser Sintering

Bin Xiao* and Yuwen Zhang†
University of Missouri–Columbia, Columbia, Missouri 65211

Partial melting and resolidification of single-component metal powders bed with a Gaussian laser beam is investigated numerically. Because laser processing of metal powder is a very rapid process, the temperature of the liquid layer and solid core of a partially molten particle may not at thermal equilibrium, that is, the temperature of the liquid part is higher while the temperature of the solid core is lower than the melting point. To use an equilibrium model to describe melting of single-component metal powder, the local temperature of regions with partially molten particles can be assumed to be within a range of temperature adjacent to the melting point, instead of at the melting point. In addition, the whole powder bed shrinks as the gas is driven out during the melting process. A temperature transforming model is employed to simulate the melting and resolidification process over a temperature range with the consideration of shrinkage. The convection driven by capillary and gravity forces in the melting liquid pool is formulated by using Darcy's law. Effects of laser beam intensity and scanning velocity on the shape and size of the heat affected zone and molten pool are analyzed.

Nomenclature

B	=	dimensionless source term
Bi	=	Biot number
Bo	=	Bond number
b	=	source term
C	=	dimensionless heat capacity
C_ℓ	=	heat capacity, J/m^3 · K
c_p	=	specific heat, J/kg · K
d_p	=	diameter of the solid core of the powder particle, m
g	=	gravitational acceleration
$h_{s\ell}$	=	latent heat of melting or solidification, J/kg
K	=	dimensionless thermal conductivity or permeability, m^2
$K_{r\ell}$	=	relative permeability
k	=	thermal conductivity, W/m · K
$\boldsymbol{k}$	=	unit vector in the z direction
Ma	=	Marangoni number
N_i	=	dimensionless moving laser beam intensity
N_R	=	radiation number
N_t	=	temperature ratio
P	=	laser power, W
P_c	=	dimensionless capillary pressure
p_c	=	capillary pressure, N/m^2
R	=	radius of the laser beam, m
S	=	dimensionless location of interface between solid and mushy zones
S_0	=	dimensionless location of heating surface
s	=	location of interface between solid zone and mushy zone, m
s_0	=	location of surface, m
T	=	temperature, K
t	=	time, s
U	=	dimensionless liquid velocity in the X direction
U_b	=	dimensionless scanning velocity of laser beam
u	=	liquid velocity in the x direction, m/s
u_b	=	scanning velocity of the laser beam, m/s
V	=	volume, m^3, or dimensionless liquid velocity in the Y direction
v	=	liquid velocity in the y direction, m/s
W	=	dimensionless liquid velocity in the Z direction
W_s	=	dimensionless velocity induced by shrinkage
w	=	liquid velocity in the z direction, m/s
w_s	=	velocity induced by shrinkage, m/s
X, Y, Z	=	dimensionless coordinates
x, y, z	=	coordinates, m
α	=	thermal diffusivity, m^2/s
α_a	=	absorptivity
ΔT	=	one-half of phase change temperature range, K
$\Delta\theta$	=	one-half of dimensionless phase change temperature range
ε	=	porosity (volume fraction of void), $(V_g + V_\ell)/(V_g + V_\ell + V_s)$
ε_e	=	emissivity
θ	=	dimensionless temperature
μ	=	dynamic viscosity, kg/m · s
ρ	=	density, kg/m^3
σ	=	Stefan–Boltzman constant, 5.67×10^{-8} W/m^2 · K^4
τ	=	dimensionless time
φ_g	=	volume fraction of gas, $V_g/(V_g + V_\ell + V_s)$
φ_ℓ	=	volume fraction of liquid, $V_\ell/(V_g + V_\ell + V_s)$
φ_s	=	volume fraction of solid, $V_s/(V_g + V_\ell + V_s)$
ψ	=	saturation

Subscripts

eff	=	effective
f	=	fusion
g	=	gas
p	=	powder material
s	=	solid

Received 27 May 2005; revision received 28 July 2005; accepted for publication 1 August 2005.

*Graduate Research Assistant, Department of Mechanical and Aerospace Engineering.
†Associate Professor, Department of Mechanical and Aerospace Engineering. Senior Member AIAA.

I. Introduction

EMERGING in the late 1980s, rapid prototyping is termed as a class of technologies, such as stereolithography,[1] laminated object manufacturing,[2] and fused deposition modeling,[3] by which complex, convoluted, and near-impossible shapes can be automatically constructed from computer-aided design data in a short time. Selective laser sintering[4–6] (SLS) is one of the rapid prototyping technologies allowing fabrication of three-dimensional freeform

objects directly from polycarbonate, nylon, and metal powder with a scanning laser beam. Various modelings have been explored by researchers to understand the physical mechanism during the complex SLS process. In the early literature, the sintering process was modeled as a pure conduction problem[7–11] that is applicable to the sintering of amorphous polymeric material because it has little crystallinity and a near zero latent heat of fusion during melting.

Heat conduction in a semi-infinite region or finite slab with moving heat source has been investigated intensively in the past. Cline and Anthony[7] examined the heat conduction problem using Green's function for a Gaussian beam moving at a constant velocity. Moody and Hendel[8] numerically investigated the temperature distribution in an infinite medium during laser heating. Kant[9] studied the heating of a multilayered cylindrical medium resting on a half-space with a stationary laser beam. Modest and Abakians[10] examined the heat conduction in a moving semi-infinite solid under a pulsed, penetrating, Gaussian laser source. Kar and Mazumder[11] presented a three-dimensional transient thermal analysis on finite slabs moving at a constant velocity by considering temperature-dependent thermophysical properties and laser irradiation with a Gaussian beam.

In contrast with SLS of amorphous polymeric materials, the latent heat of fusion in metal SLS is usually very large, and therefore, melting and resolidification have significant effects on the temperature distribution during sintering. In addition, convective flow in the molten pool strongly influences the energy transport, the propagation of the melting front during the metal SLS process. Recently quantitative mathematical studies of metal SLS have been carried out by researchers taking into consideration of convection effect. Pak and Plumb[12] presented a one-dimensional model of melting in a two-component powder bed with consideration of the liquid motion driven by gravity and capillary forces. The study showed that the constant porosity model yielded results that compared well with the experimental data. Iwamoto et al.[13] examined a computational model describing the mechanism for the formation of topographic features during pulsed laser texturing of metal substrates by focused laser beams. Capillary forces acting on the surface of the molten material and driven by temperature gradients were shown to produce surface deformation profiles. Han and Liou[14] simulated the laser melting process for different laser beam modes. Flow pattern, which is driven mainly by the thermocapillary force and recoil pressure, together with temperature distribution are investigated and compared.

During the metal SLS process, the powder bed experiences a significant density change because the pore space initially occupied by gases is partially taken up by the liquid. The shrinkage phenomena in metal SLS caused by density change have been considered by some researchers. Zhang and Faghri[15] analytically solved a one-dimensional melting problem in a powder bed containing a powder mixture under a boundary condition of the second kind. The results showed that the shrinkage effect on the melting of the powder bed is not negligible. Zhang and Faghri[16] numerically examined the two-dimensional melting and resolidification of a subcooled mixed powder bed with moving Gaussian heat source. The results with and without shrinkage effect are compared. Furthermore, Zhang et al.[17] numerically and experimentally investigated the sintering process of two-component metal powders under irradiation of a stationary or a moving Gaussian laser beam. The liquid velocities caused by capillary and gravity forces and solid velocities caused by the shrinkage are considered.

In principle, both single- and two-component metal powders can be used in metal SLS.[18] In the case of two-component metal sintering, a liquid phase is formed by melting the lower melting point metal powders, which infiltrates into the voids between the high melting point powders and binds them together. Because the final product of two-component system exhibits the mechanical properties and characteristics of their weakest component, interest in the production of metallic objects using single-component powders has been increased in the recent years.[19–21] In the case of direct SLS of metal powders, a partial melting approach can be employed. Only the surfaces of particles are molten, and the powders are sintered by binding the solid nonmelted cores of particles. Control of solid–liquid ratio and the melt viscosity are critical in successful sintering of single-component system. Excessive molten material or too low melt viscosity causes the "balling" phenomenon,[22] which reduces the effective load-carrying capacity of a material and acts as stress concentrations and effective crack initiation sites. Thus, the parameters of laser processing must be carefully selected to ensure the partial melting.

The physical processes of the direct laser surface melting of metal powders include radiative and covective boundary conditions, thermodynamics of phase changes, a moving boundary at the heating surface and the solid–melting surface, fluid flow, and heat and mass transportation governed by thermocapillary and surface tension effects in the molten pool. This complexity of the laser surface melting process requires the construction of sophisticated models that could offer efficient and flexible means to analyze and optimize the sintering process. In this paper, a three-dimensional model is presented to simulate the direct SLS process of metal powders to better understand the partially melting mechanisms during the direct SLS process of metal powders. Because SLS is a very rapid process, the liquid layer and solid core of a partially molten powder particle may not at thermal equilibrium and have different temperatures. The mean temperature of a partially molten grain can be either below or above the melting point, depending on the degree of melting. Thus, the melting process is assumed to occur in a temperature range and the degree of melting is function of temperature in the range. The shrinkage phenomenon during the melting process is considered, and the phase change is described using a temperature transforming model. Liquid velocities induced by capillary and gravity forces and solid velocities caused by shrinkage during the melting process are also taken into consideration. Effects of laser beam intensity and scanning velocity on temperature distribution, solid fraction change, and the shapes of heat affected zone and molten pool will be investigated.

II. Physical Model

A. Problem Description

Consider a powder bed with initial temperature T_i, which is lower than the melting point, T_f, in a cavity with a size of $x_D \times 2y_D \times z_D$ (length times width times height) as shown in Fig. 1. A Gaussian laser beam scans the surface of the powder bed in the positive x direction with a constant velocity u_b. When the laser beam scans the surface of the powder bed, a partial melting region is formed under the laser beam. As will become evident later, the combination of the laser intensity and scanning velocity must be carefully selected to allow formation of the partial melting region. Inappropriate combination of the laser intensity and scanning velocity may lead to nonmelting or complete melting. After the laser beam moves away, the partial melting region cools and resolidifies to form a densified heat affect zone (HAZ). The problem under consideration is a typical moving heat source problem.[23] Because the size of heat source (on the order of 10^{-3} m) is much smaller than the size of the powder bed, the sintering process appears to be quasi-steady state from the standpoint of the observer located in and traveling with the heat source.[16] Compared with the one-dimensional model[15] that considers heat conduction in the z direction only and the two-dimensional model[16] that considers heat conduction in the x and z directions, conduction/convection heat transfer in all three directions is considered in this paper.

Because laser processing of metal powder is a very rapid process, the liquid surface of a partially molten powder particle has a higher temperature than melting point while the solid core has a temperature below the melting point.[24] Therefore, the mean temperature of a partially molten particle is within a range of temperature adjacent to the melting point, depending on the degree of melting. The liquid infiltrates into the void in the unsintered region of the powder bed, which affects the melting process and causes the density change. The nonmolten cores of the particles cannot sustain the powder bed and will move downward to cause shrinkage of the whole powder bed.

It is assumed in this paper that the degree of melting is less than or equal to the initial porosity of the loose powder, under which condition a constant porosity model can be applied. Under the constant

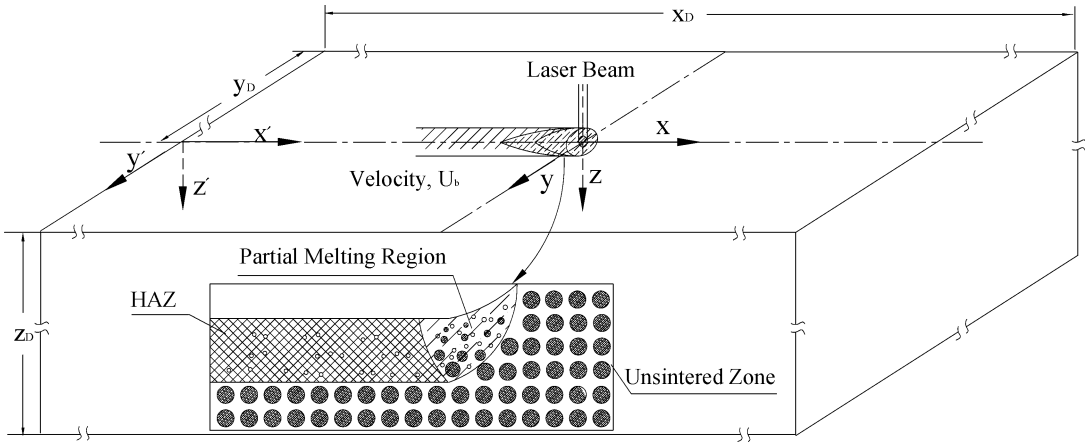

Fig. 1 Physical model.

porosity model, the volume initially occupied by the gas is taken up by the newly formed liquid. In other words, when certain volume of liquid is formed, the same volume of the gas will be driven out from the powder bed. Consequently, the powder bed volume continuously decreases during melting until all of the gas is driven out. In addition the following assumptions are made during the melting process.

1) The density, specific heat and thermal conductivities of both liquid and solid phases of the powder material are the same and are independent of the temperature.

2) The contribution of the gas to the density and heat capacity to the powder bed is negligible.

3) The velocity of the solid induced by the shrinkage of the powder bed is only in the z direction whereas the liquid flows in all three directions.

B. Velocities and Fractions in Partial Melting Region

Once partial melting in the powder bed is initiated, the volume initially occupied by the gas will be partially taken up by the liquid because only solid can sustain the powder structure. The porosity, defined as the total volume of void, including the volumes of gas and liquid, relative to the total volume occupied by the solid matrix and void volume $[\varepsilon = (V_\ell + V_g)/(V_\ell + V_g + V_s) = \varphi_g + \varphi_\ell]$ (Ref. 24), remains constant, whereas the volume of the bed continuously changes because the gas is driven out by the liquid generated during melting. In other words, the volume of the gas driven out from the powder bed is equal to the volume of liquid produced during partial melting to maintain a constant porosity. The shrinkage accompanying the partial melting will induce a downward velocity in the z direction.

As described in Sec. II.A, the constant porosity model is valid only before the gas in the powder bed is fully driven out, that is, the solid fraction f in the powder bed is less than or equal to $1 - \varepsilon$ (Ref. 25). This particular case is chosen because the ratio of solid and liquid is sufficient to avoid the occurrence of the balling phenomenon. The solid fraction $f(T)$ varies from zero in the fully liquid region and one in the unmelting solid region and is assumed to be linear function of the local temperature T by

$$f = \begin{cases} 1, & T < T_f - \Delta T \\ (T_f + \Delta T - T)/2\Delta T, & T_f - \Delta T < T < T_f + \Delta T \\ 0, & T > T_f + \Delta T \end{cases} \tag{1}$$

where $2\Delta T$ is the temperature range of melting.

Because the porosity ε is a constant in the constant porosity model, the volume fraction of unmelted solid, $\varphi_s = 1 - \varepsilon$, remains unchanged during partial melting. According to the definitions of the solid mass fraction, $f = \rho_p V_s/(\rho_p V_s + \rho_p V_\ell)$, and the liquid volume fraction, $\varphi_\ell = V_\ell/(V_s + V_\ell + V_g)$, the following equation can be obtained:

$$\varphi_\ell = (1 - f)\varphi_s/f = (1 - f)(1 - \varepsilon)/f \tag{2}$$

The liquid velocities must satisfy the following continuity equation:

$$\frac{\partial(\varphi_\ell + \varphi_s)}{\partial t} + \nabla \cdot (\varphi_\ell \boldsymbol{v}_\ell) + \frac{\partial(\varphi_s w_s)}{\partial z} = 0 \tag{3}$$

Substituting $\varphi_s = 1 - \varepsilon$ into Eq. (3), one obtains

$$\frac{\partial \varphi_\ell}{\partial t} + \nabla \cdot (\varphi_\ell \boldsymbol{v}_\ell) + (1 - \varepsilon)\frac{\partial w_s}{\partial z} = 0 \tag{4}$$

Darcy's law is utilized to obtain the liquid velocities in three directions,

$$\boldsymbol{v}_\ell - w_s \boldsymbol{k} = (K K_{r\ell}/\varphi_\ell \mu)(\nabla p_c + \rho_\ell g \boldsymbol{k}) \tag{5}$$

The permeability K is related to the diameter of the solid core d_p and porosity ε by the Carman–Kozeny equation (see Ref. 17),

$$K = \frac{d_p^2 \varepsilon^3}{180(1 - \varepsilon)^2} \tag{6}$$

The relative permeability $K_{r\ell}$ is equal to ψ_e^3 (Ref. 17), where ψ_e is the normalized saturation defined as

$$\psi_e = \begin{cases} (\psi - \psi_{ir})/(1 - \psi_{ir}), & \psi > \psi_{ir} \\ 0, & \psi \le \psi_{ir} \end{cases} \tag{7}$$

The capillary pressure is $p_c = [1.417(1 - \psi_e) - 2.12(1 - \psi_e)^2 + 1.263(1 - \psi_e)^3]\gamma^0\sqrt{(\varepsilon/K)}$ (Ref. 26), where the surface tension of liquid metal, γ^0, is expressed as a linear function of temperature, $\gamma^0 = \gamma_m[1 - \gamma^{0'}(T - T_f)]$ (Ref. 17).

C. Energy Equation

The temperature transforming model, which combines the advantages of the enthalpy model and equivalent heat capacity models, is used to describe the heat transfer process during melting and resolidification.[27] The energy equation for the physical problem is

$$\frac{\partial}{\partial t}[(\varphi_\ell + \varphi_s)C_\ell T] + \nabla \cdot (\varphi_\ell \boldsymbol{v}_\ell C_\ell T) + \frac{\partial}{\partial z}(\varphi_s w_s C_\ell T) = \nabla \cdot (k \nabla T) - \left\{ \frac{\partial}{\partial t}[(\varphi_\ell + \varphi_s)b] + \nabla \cdot (\varphi_\ell \boldsymbol{v}_\ell b) + \frac{\partial}{\partial z}(\varphi_s w_s b) \right\} \tag{8}$$

The effective heat capacity can be expressed as

$$c_\ell = \begin{cases} \rho_p c_p, & T \le T_f - \Delta T \\ \rho_p c_p + \rho_p h_{s\ell}/2\Delta T, & T_f - \Delta T < T < T_f + \Delta T \\ \rho_p c_p, & T \ge T_f + \Delta T \end{cases} \tag{9}$$

and b in Eq. (8) is defined as

$$b = \begin{cases} 0, & T \le T_f - \Delta T \\ \frac{1}{2}\rho_p h_{s\ell}, & T_f - \Delta T < T < T_f + \Delta T \\ \rho_p h_{s\ell}, & T \ge T_f + \Delta T \end{cases} \tag{10}$$

The thermal conductivity of the powder bed is calculated by

$$k = \begin{cases} k_{\text{eff}}, & T \le T_f - \Delta T \\ k_{\text{eff}} + \dfrac{k_\ell - k_{\text{eff}}}{2\Delta T}(T - T_f + \Delta T), & T_f - \Delta T < T < T_f + \Delta T \\ k_\ell, & T \ge T_f + \Delta T \end{cases} \tag{11}$$

where k_{eff} is the effective thermal conductivity of the unsintered powder bed. It can be calculated using the empirical correction proposed by Hadley.[28] When melting begins, the liquid infiltrated between the unmelted cores of the particles and the contact area is significantly increased. The thermal conductivity of the partial melting region and resolidified part is, therefore, calculated using

$$k_\ell = (\varphi_\ell + \varphi_s)k_p \tag{12}$$

Because the heating domain is much larger compared with the size of the laser beam, the heat source in the center of the domain is far away and has an insignificant effect on the sides and the bottom of the domain. Thus, the boundary and initial conditions of the energy equation can be described as

$$-k\frac{\partial T}{\partial z} = \frac{\alpha_a P}{\pi R^2}\exp\left[-\frac{x^2+y^2}{R^2}\right] - \varepsilon_e\sigma\left(T^4 - T_\infty^4\right) - h(T - T_\infty) \tag{13a}$$

$$\frac{\partial T}{\partial z} = 0, \qquad z = z_D \tag{13b}$$

$$\frac{\partial T}{\partial x} = 0, \qquad x = 0, x_D \tag{13c}$$

$$\frac{\partial T}{\partial y} = 0, \qquad y = 0, y_D \tag{13d}$$

$$T = T_i, \qquad t = 0 \tag{13e}$$

D. Dimensionless Governing Equations

When the following dimensionless variables

$$\tau = \frac{\alpha_p t}{R^2}, \qquad X, Y, Z = \frac{(x, y, z)}{R}, \qquad \theta = \frac{T - T_f}{T_f - T_i}$$

$$\Delta\theta = \frac{\Delta T}{T_f - T_i}, \qquad K = \frac{k}{k_p}, \qquad K_{\text{eff}} = \frac{k_{\text{eff}}}{k_p}$$

$$C = \frac{(\varphi_\ell + \varphi_s)C_\ell}{\rho c_p}, \qquad B = \frac{(\varphi_\ell + \varphi_s)b}{c_p(T_f - T_i)}, \qquad U = \frac{\varphi_\ell u_\ell R}{\alpha_p(\varphi_\ell + \varphi_s)}$$

$$U_b = \frac{u_b R}{\alpha_p}, \qquad V = \frac{\varphi_\ell v_\ell R}{\alpha_p(\varphi_\ell + \varphi_s)}, \qquad W = \frac{(\varphi_\ell w_\ell + \varphi_s w_s)R}{\alpha_p(\varphi_\ell + \varphi_s)}$$

$$P = \frac{p}{\gamma_m\sqrt{\varepsilon/k}}, \qquad Sc = \frac{c_p(T_f - T_i)}{\rho h_{s\ell}}, \qquad N_i = \frac{P\alpha_a}{Rk_p(T_f - T_i)}$$

$$Bi = \frac{hR}{k_p}, \qquad N_R = \frac{\varepsilon_e\sigma(T_f - T_i)^3 R}{\pi R k_p(T_f - T_i)}, \qquad N_t = \frac{T_f}{T_f - T_i} \tag{14}$$

are defined, the energy equation (8) is nondimensionalized as

$$-U_b\frac{\partial(C\theta)}{\partial X} + \frac{\partial(UC\theta)}{\partial X} + \frac{\partial(VC\theta)}{\partial Y} + \frac{\partial(WC\theta)}{\partial Z} = \frac{\partial}{\partial X}\left(K\frac{\partial\theta}{\partial X}\right) + \frac{\partial}{\partial Y}\left(K\frac{\partial\theta}{\partial Y}\right) + \frac{\partial}{\partial Z}\left(K\frac{\partial\theta}{\partial Z}\right) - \left\{-U_b\frac{\partial B}{\partial X} + \frac{\partial(UB)}{\partial X} + \frac{\partial(VB)}{\partial Y} + \frac{\partial(WB)}{\partial Z}\right\} \tag{15}$$

where

$$C = \begin{cases} (\varphi_\ell + \varphi_s), & \theta \le -\Delta\theta \\ (\varphi_\ell + \varphi_s)(1 + 1/2Sc\Delta\theta), & -\Delta\theta < T < \Delta\theta \\ (\varphi_\ell + \varphi_s), & \theta \ge \Delta\theta \end{cases} \tag{16}$$

$$B = \begin{cases} 0, & \theta \le -\Delta\theta \\ (\varphi_\ell + \varphi_s)/2Sc, & -\Delta\theta < T < \Delta\theta \\ (\varphi_\ell + \varphi_s)/Sc, & \theta \ge \Delta\theta \end{cases} \tag{17}$$

$$K = \begin{cases} K_{\text{eff}}, & \theta \le -\Delta\theta \\ K_{\text{eff}} + \{[(\varphi_\ell + \varphi_s) - K_{\text{eff}}]/2\Delta\theta\}(\theta + \Delta\theta), & -\Delta\theta < T < \Delta\theta \\ (\varphi_\ell + \varphi_s), & \theta \ge \Delta\theta \end{cases} \tag{18}$$

The dimensionless velocity of the mushy zone is calculated by the dimensionless form of Eq. (5), that is,

$$\boldsymbol{V}_\ell - W_s\boldsymbol{k} = \frac{\varepsilon Ma\psi_e^3}{\sqrt{180}(1-\varepsilon)\psi}\nabla P_c + \frac{\varepsilon^2 MaB_o\psi_e^3}{180(1-\varepsilon)^2\psi}\boldsymbol{k} \tag{19}$$

Equation (19) should satisfy the nondimensional continuity equation of the mushy zone, which can be obtained by nondimensionalizing Eq. (4),

$$\frac{\partial\varphi_\ell}{\partial\tau} + \nabla\cdot(\varphi_\ell\boldsymbol{V}_\ell) + (1-\varepsilon)\frac{\partial W_s}{\partial Z} = 0 \tag{20}$$

The boundary condition at the top surface of the powder bed [Eq. (13a)] is nondimensionalized as

$$-K\frac{\partial\theta}{\partial\tau} = \frac{N_i}{\pi}\exp[-X^2 - Y^2] - N_R\left[(\theta + N_t)^4 - (\theta_\infty + N_t)^4\right] - B_i(\theta - \theta_\infty)$$

$$Z = S_0(X, Y) \tag{21}$$

The dimensionless form of the other equations can also be obtained using the dimensionless variables defined in Eq. (14).

III. Numerical Solution

The melting and resolidfication problem governed by Eqs. (15–21) is a steady-state, three-dimensional, nonlinear problem. Because the locations of the solid–liquid interface and the surface of mushy zone are unknown a priori, a false transient method is employed to locate various interfaces. Steady-state solution is declared when the temperature distribution and locations of various interfaces do not vary with the false time. Equation (15) with the false transient term can be solved by the finite volume method.[29] The computational domain is the whole powder bed, and a block-off technique[29] is employed to simulate the existence of the empty space created by shrinkage of the powder bed after partial melting. The density and thermal conductivity in the empty space are set to be zero. The power-law scheme is applied to discretize the convection/diffusion terms.

Because of axisymmetry with respect to the center plan, $Y = 0$, the velocity and temperature fields were calculated on only one side of the center plan, $Y > 0$. The analysis of the sintering process involves solutions of 1) the velocities and the volume fractions of the solid particles, 2) the velocities and the volume fractions of the

liquid, and 3) the temperature distribution and the location of the surface of mushy zone, the solid–liquid interface, and the sintering interface. Because Eqs. (15), (19), and (20) are conjugated, an iterative solution procedure with underrelaxation is employed, and the underrelaxation factor is 0.2. The grid number used in computation is $122 \times 52 \times 122$ (in the X, Y, and Z directions, respectively), and the false time step is 0.1. A nonuniform grid was used, that is, fine grids near the heat source and coarse grid away from the center of the laser beam.

IV. Results and Discussions

The porosity of the unsintered powder bed plays an important role because the thermal properties of the powder bed depend on the value of the porosity. For uniform-sized spherical particles, the porosity is independent of the particle size but relates to only the structural arrangement of the particles in the powder bed. For simple-cubic (6 contact points), face-centered-cubic (8 contact points), and body-centered-cubic (12 contact points) close-pack arrangements, the porosities are 0.476, 0.32, and 0.26, respectively. For randomly packed powder bed, the porosity is around 0.4 (Ref. 26). Therefore, the initial porosity of the unsintered powder bed is set as 0.4.

To demonstrate the validity of the simulation code, numerical simulation of temperature distribution for pure conduction in the powder bed with a moving laser beam is performed to compare with the analytical solution for the pure conduction in a semi-infinite body with a moving point heat source,[30]

$$T_s - T_i = (P\alpha_a/2\pi k_{\text{eff}} r)\exp[-u(r+x)/2\alpha] \tag{22}$$

When the dimensionless variables defined in Eq. (14) are used, the dimensionless form of Eq. (22) can be rewritten as

$$\theta + 1 = \frac{N_i}{2\pi K_{\text{eff}} R}\exp\left[-\frac{(1-\varepsilon)U_b(R+X)}{2K_{\text{eff}}}\right] \tag{23}$$

where $R = \sqrt{(X^2+Y^2+Z^2)}$.

To simulate the conduction problem in the powder bed with a moving point heat source on the surface, the Gussian distribution laser beam is replaced by a top-hat (uniform distribution) laser beam because the former one diffuses the energy in a wide circle. Thus, the boundary condition in Eq. (21) is changed to the following equation:

$$-K_{\text{eff}}\frac{\partial\theta}{\partial Z} = \begin{cases} N_i, & Z=0 \quad \sqrt{X^2+Y^2} \le 1, \quad \tau > 0 \\ 0, & Z=0 \quad \sqrt{X^2+Y^2} > 1, \quad \tau > 0 \end{cases} \tag{24}$$

As can be seen from Fig. 2, the agreement between the numerical and analytical solutions is very good, except for the area around $X = 0$. This deviation is caused by the difference between the two heat sources used in the numerical and analytical models. The one used in analytical model is infinitesimal, whereas the one used in the numerical model is of finite size. When the differences of the size of the heat sources used in the numerical and analytical solutions are considered, the overall agreement between the numerical and analytical solution is good.

Numerical calculation is performed for sintering of AISI 304 stainless steel powder. Table 1 lists the material physical properties for AISI 304.[31,32] The range of melting temperature $2\Delta T$ is related to the properties of the material, heat flux, and heating time. Accurate determination of the phase change temperature range can only be obtained by modeling of the powder particle that goes through melting and resolidification, which is under investigation. To demonstrate the capability of the partial shrinkage model developed in this paper, numerical simulation is performed using a range of the melting temperature of 160°C. To minimize the balling effect and geometric distortion (curling or delaminating), a preheated powder bed with initial temperature of 380°C is used in the simulation, and the corresponding subcooling parameter is $Sc = 2.0$. At lower intensity and higher scanning velocity, the powders will not be sintered at all or poorly sintered. On the other hand, at higher intensity and lower scanning velocity, the entire powder will be liquefied and the balling phenomena will appear. Because partial melting of the powder particle is desirable, selection of laser processing parameters must be strict to ensure not complete but only surface melting of particles. Therefore, the heat source intensity and the scan velocity at which sintering occurs vary over a narrow range. To keep enough liquid–solid ratio and sintering depth, the dimensionless intensity and the scanning velocity are assumed to vary from 0.19 to 0.20 and 0.12 to 0.24, respectively, in the present study.

Figure 3 shows the surface temperature distribution of the powder bed. The dimensionless intensity of the laser beam, N_i, is 0.19 and the dimensionless scanning velocity U_b is 0.12. Note that the peak temperature at the powder bed surface is near the trailing edge of the laser beam rather than at the center of the laser beam due to

Table 1 Thermophysical properties of AISI 304

Property	Symbol	Unit	Value
Density	ρ_p	kg/m^3	7200
Thermal conductivity	k_p	W/m · K	14.9
Specific heat	c_p	J/kg · K	462.6
Melting point	T_f	K	1670
Latent heat of fusion	$h_{s\ell}$	kJ/kg	247
Viscosity	μ	kg/s · m	0.05
Surface tension at melting point	γ	N/m	1.943

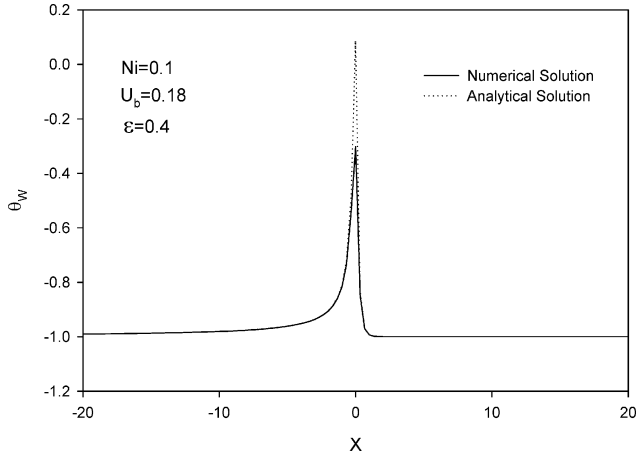

Fig. 2 Comparison between analytical and numerical solutions for pure conduction.

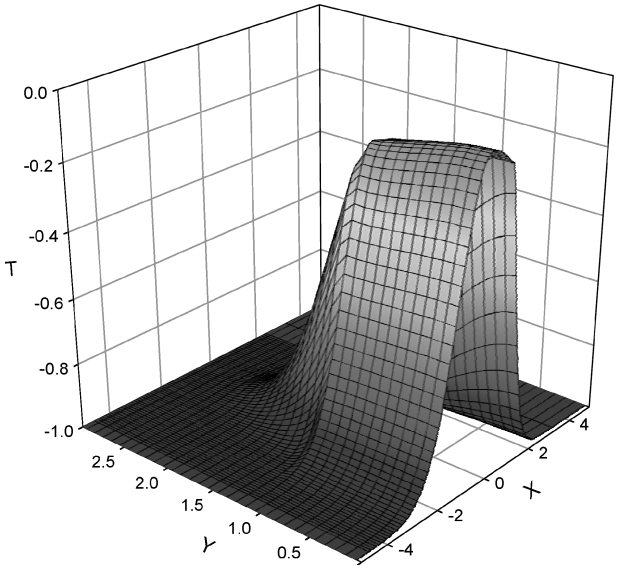

Fig. 3 Three–dimensional surface temperature distribution on the powder bed surface; $N_i = 0.19$ and $U_b = 0.12$.

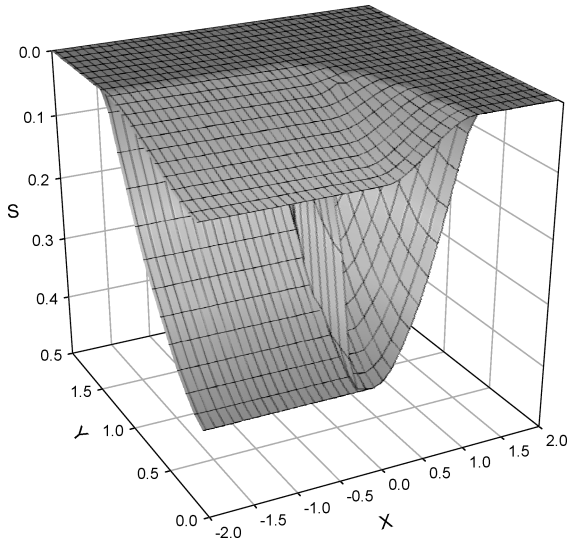

Fig. 4 Three-dimensional shape of HAZ; $N_i = 0.19$ and $U_b = 0.12$.

motion of the laser beam. Because the thermal conductivity in the molten pool is much larger than that in the unsintered zone, the temperature changes smoothly in the molten pool, whereas sharply in the unsintered zone near the molten pool. Figure 4 shows the three-dimensional shape of the powder bed surface, molten pool, and HAZ subjected to irradiation of a moving laser beam in the moving coordinates system at the same condition of Fig. 3. The shrinkage at the track of the center of the laser beam is most significant and a groove is formed on the surface of the powder bed. In addition, the depths of surface and HAZ decrease with the increasing X in the laser scanning direction Y.

Figure 5a and 5b show the contour of solid fraction at the surface of the powder bed and the X–Z plane in the same condition as Fig. 3. The solid fraction in the liquid pool represents the mass fraction of the unmelted solid in the total mass of the powder materials. In the resolidified region that contains resolidified solid and the solid core that did not undergo melting and resolidification, the solid fraction represents the fraction of solid did not undergo melting and resolidification. It can be seen from Fig. 5a that the solid fraction contour is in a horseshoe shape. The solid fraction near the center of the laser beam is lowest where the degree of melting is highest. As required by the constant porosity model, the shrinkage at the center

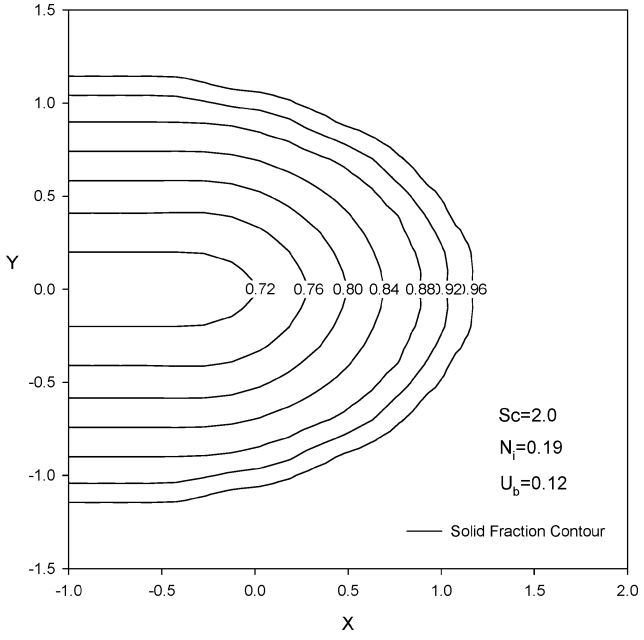

a) Powder bed surface

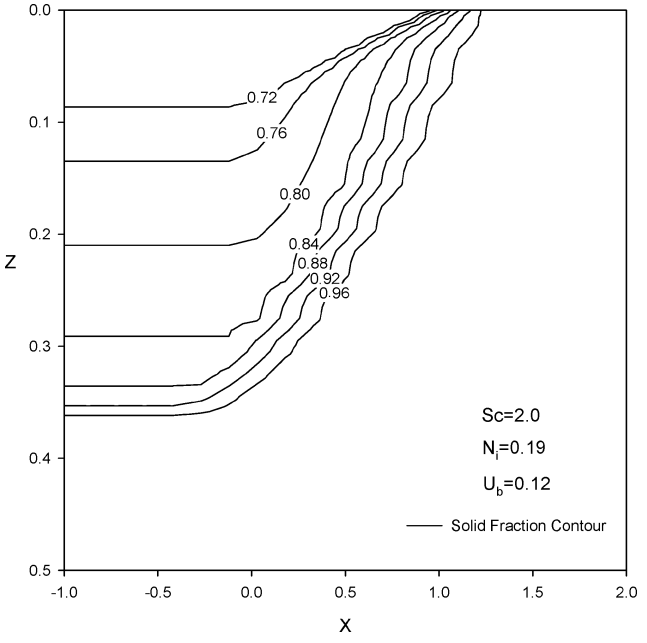

b) X–Z plane

Fig. 5 Contour of solid fraction; $N_i = 0.19$ and $U_b = 0.12$.

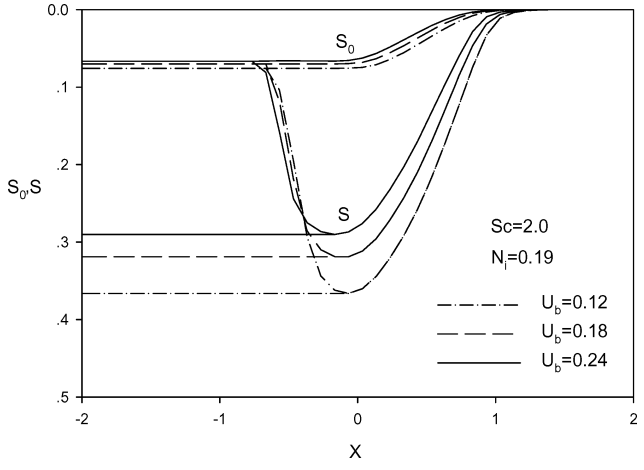

a) X–Z plane

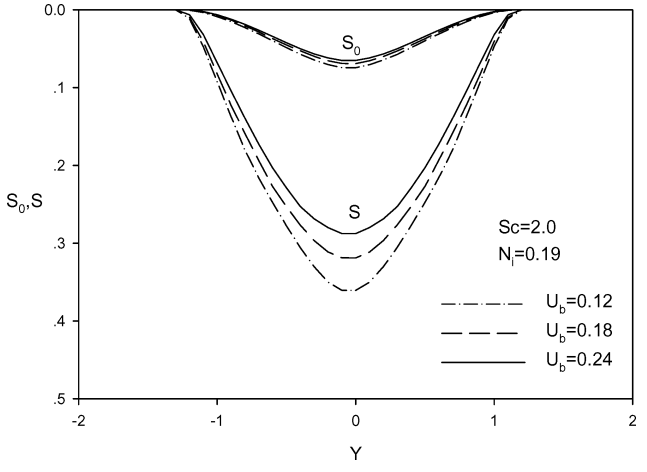

b) X–Y plane

Fig. 6 Cross-sectional shape of surface, molten pool and HAZ; $N_i = 0.19$.

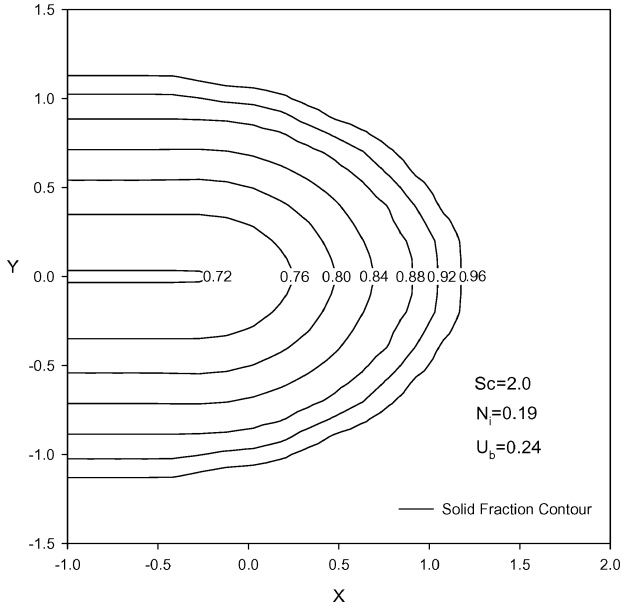

a) Powder bed surface

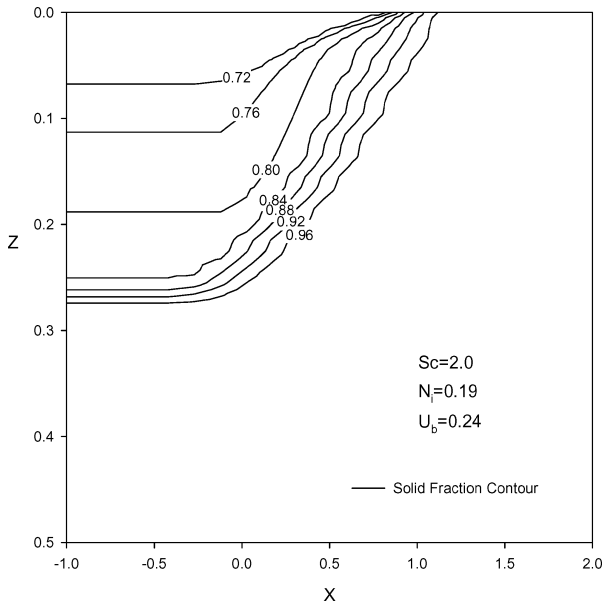

b) *X–Z* plane

Fig. 7 Contour of solid fraction; $N_i = 0.19$ and $U_b = 0.24$.

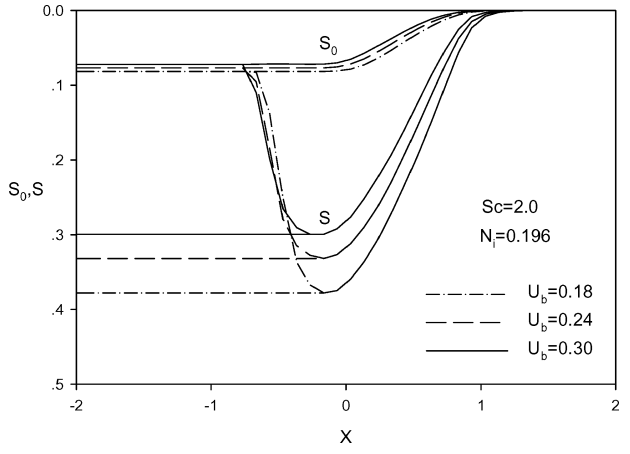

a) *X–Z* plane

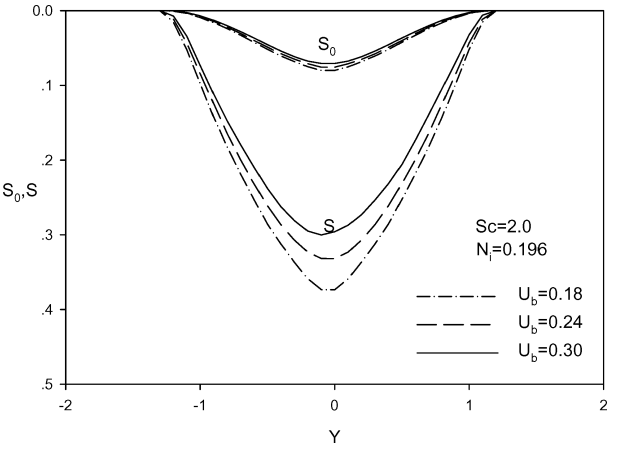

b) *X–Y* plane

Fig. 8 Cross-sectional shape of surface, molten pool, and HAZ; $N_i = 0.196$.

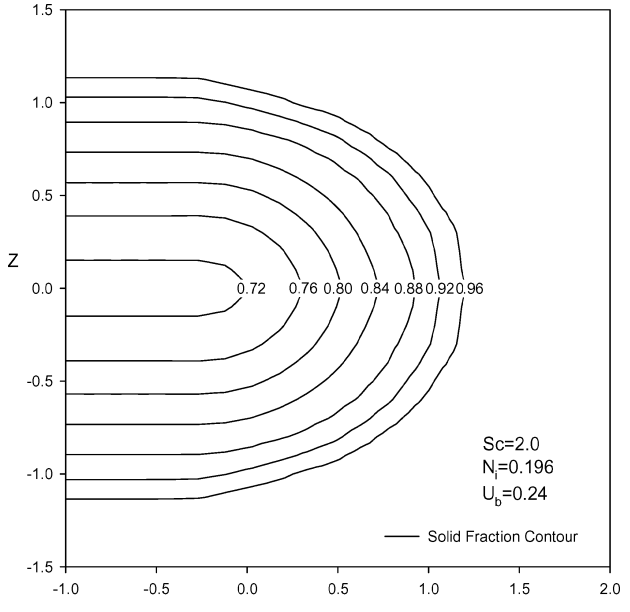

a) Powder bed surface

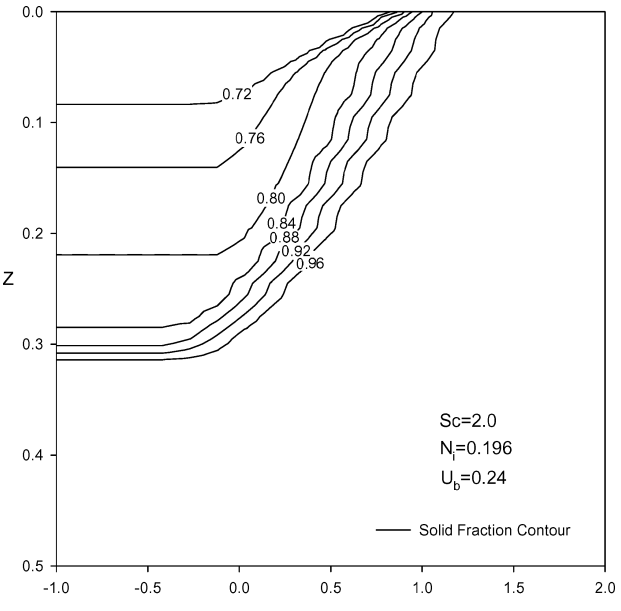

b) *X–Z* plane

Fig. 9 Contour of solid fraction; $N_i = 0.196$ and $U_b = 0.24$.

of the laser beam is also the most significant. As the result of the laser scanning, what is left behind the laser beam on the surface of the powder bed is a groove (Fig. 4) and the density of the HAZ at the bottom of the groove is highest. The solid fraction contour in the X–Z plane is shown in Fig. 5b. It can be seen that the solid fraction near the surface of the heat affected zone is the lowest because the degree of melting at the surface is highest.

Figures 6a and 6b show the cross-sectional shapes of surface, molten pool, and HAZ at the X–Z and X–Y planes at $N_i = 0.19$. Note that the depths of the surface and HAZ decrease and the molten pool becomes narrower with the increasing scanning velocity because the interaction time between the moving heat source and the powder surface is decreased when the heat source moves faster. In the meantime, the whole molten pool moves toward the opposite direction of the laser scanning as the scanning velocity increases. Figures 7a and 7b show the contour of the solid fraction at the surface of the powder bed and the X–Z plane at $N_i = 0.19$ and $U_b = 0.24$. Compared with Fig. 5, the solid fraction contour shifts toward the opposite direction of the laser scanning because of the enhanced advection flow caused by the increasing scanning velocity. Because the interaction time of the laser beam and powder bed surface shortens with the increasing scanning velocity, the degree of melting decreases, and so the curve with equal solid fraction near the center of the laser beam, such as $f_s = 0.72$, is pushed inward.

Figures 8a and 8b show the cross-sectional shapes of surface, molten pool, and HAZ at the X–Z and X–Y planes at $N_i = 0.196$. Similar to the trend demonstrated in Fig. 6, the depths of surface, molten pool, and HAZ decrease and the molten pool becomes narrower with the increasing scanning velocity. The whole molten pool shifts toward the opposite direction of the laser scanning as the scanning velocity increases. The sintering depth increases with the increasing laser intensity compared with Fig. 6. Because shrinkage is assumed to occur in the Z direction only, the increase of the depth of the molten pool is much more significant than the increase of the molten pool width in the Y direction. Figures 9a and 9b show the contour of solid fraction at the powder bed surface and the X–Z plane at $N_i = 0.196$ and $U_b = 0.24$. Compared with Fig. 7, as the laser intensity increases, more solid is melted; thus, the curve with equal solid fraction near the center of the laser beam, such as $f_s = 0.72$, is pushed outward.

Figures 10a and 10b show the cross-sectional shapes of surface, molten pool, and HAZ in the X–Z and X–Y planes at $N_i = 0.2$. Trends similar to those shown in Figs. 6 and 8 can be observed in Fig. 10. Figures 11a and 11b show the contour of solid fraction in

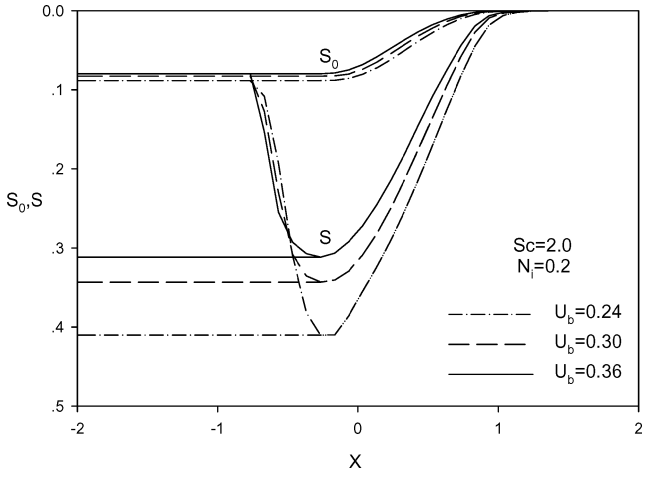

a) X–Z plane

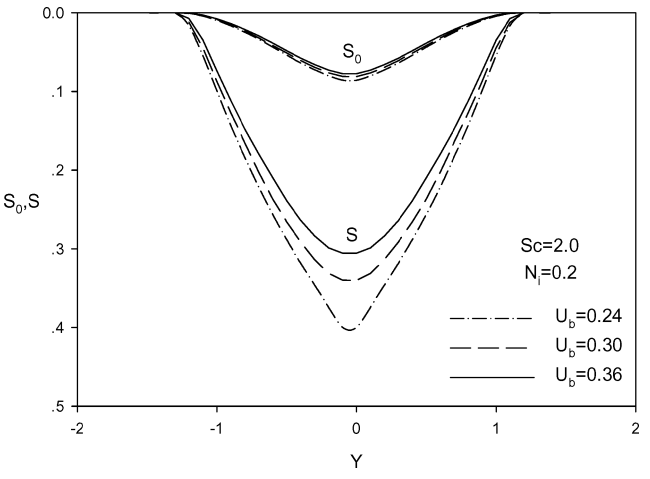

b) X–Y plane

Fig. 10 Cross-sectional shape of surface, molten pool, and HAZ; $N_i = 0.20$.

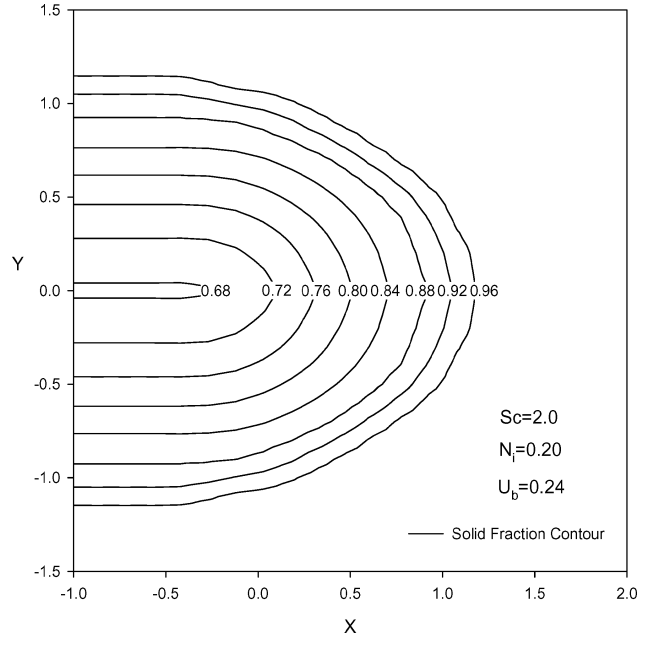

a) Powder bed surface

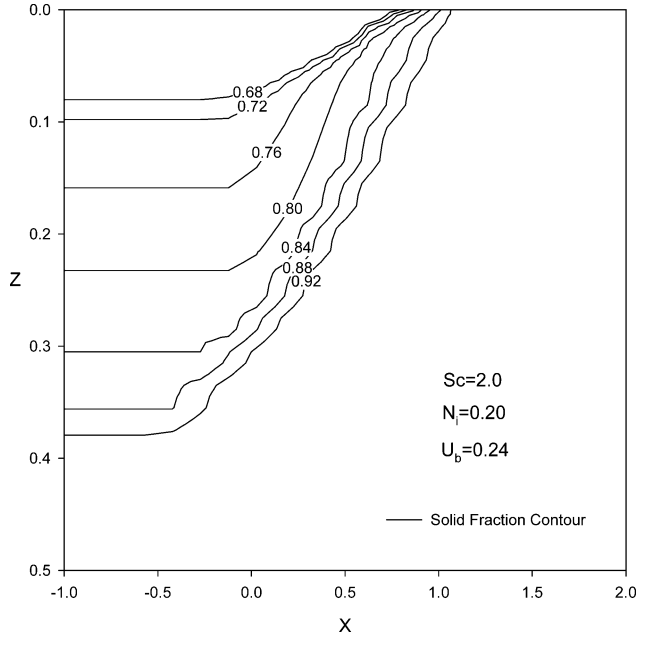

b) X–Z plane

Fig. 11 Contour of solid fraction; $N_i = 0.20$ and $U_b = 0.24$.

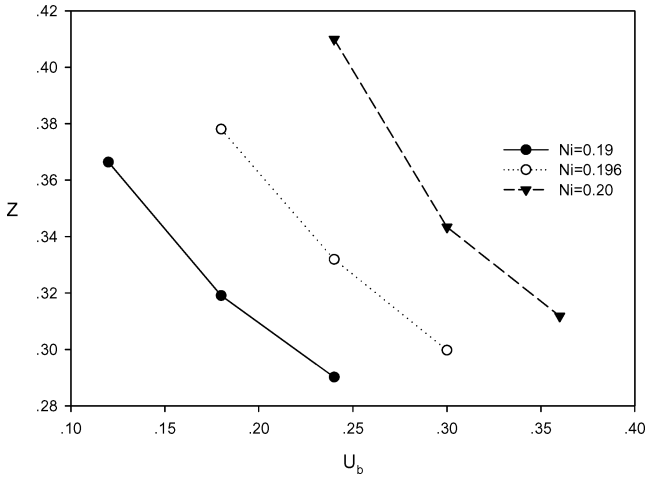

Fig. 12 Sintering depths at different laser intensities and scanning velocities.

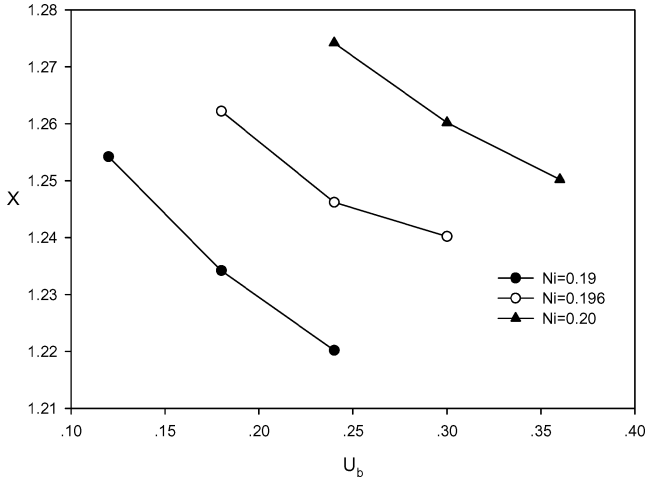

Fig. 13 Leading edges at different laser intensities and scanning velocities.

surface of the powder bed and X–Z plane at $N_i = 0.2$ and $U_b = 0.24$. Compared with Fig. 9, as the laser intensity increases, more solid is melted; thus, the curve with equal solid fraction near the center of the laser beam such as $f_s = 0.72$ is pushed outward.

Figures 12 and 13 show the sintering depths and leading edge of the molten pool with respect to the laser beam position (at $Y = 0$) for different scanning velocities and laser intensity. Note that the leading edges and sintering depth increase with increasing laser intensity or decreasing scanning velocity. At fixed laser intensity, reduced scanning velocity leads to increased laser–powder interaction time and ultimately results in greater sintering depth and farther leading edge. On the other hand, when the scanning velocity, that is, the laser–powder interaction time is fixed, increasing laser intensity results in greater sintering depth and farther leading edges because the amount of laser energy delivered to the powder bed is increased. It can be seen from Figs. 12 and 13, because of the shrinkage effect, the sintering depth moves faster than the leading edge does when the laser intensity increases or scanning velocity decreases.

V. Conclusions

Three-dimensional sintering of single-component metal powder by partial melting with a moving laser beam is investigated numerically. Because the liquid and solid of the partially molten particles during the sintering process is not at the same temperature, melting during sintering is assumed to occur over a range of temperature instead of a fixed point. Numerical simulation of sintering of AISI 304 powder is carried out, and a parametric study is performed. The results showed that the laser intensity and scanning velocity play important roles in the temperature distribution, the shapes of the sintering depth, and the solid fraction distribution. Increasing laser intensity resulted in the increments of the sintering depth and the volume of the molten pool and the depth of molten pool moves faster than the width of the molten pool because the shrinkage of the powder bed enhances the heat transportation in Z direction. Increasing scanning velocity will decrease the depth of of the surface and HAZ, narrow the molten pool, and shift the whole molten pool in the opposite direction of the increasing laser scanning velocity because the laser–material interaction time is shortened and heat advection flow increases as the laser beam moves faster.

Acknowledgment

Support for this work by the Office of Naval Research under Grant N00014-04-1-0303 is gratefully acknowledged.

References

[1]Griffith, M. L., Chu, T. M., Wagner, W. C., and Halloran, J. W., "Ceramic Stereolighography for Investment Casting and Biomedical Applications," *Proceedings of Solid Freeform Fabrication Symposium*, Univ. of Texas, Austin, TX, 1995, pp. 31–38.

[2]Griffin, C., Daufenbach, J., and McMillin, S., "Solid Freeform Fabrication of Functional Ceramic Components Using a Laminated Object Manufacturing Technique," *Proceedings of Solid Freeform Fabrication Symposium*, Univ. of Texas, Austin, TX, 1994, pp. 17–24.

[3]Bellini, A., and Guceri, S., "Mechanical Characterization of Parts Fabricated Using Fused Deposition Modeling," *Rapid Prototyping Journal*, Vol. 9, No. 4, 2003, pp. 252–264.

[4]Deckard, C. R., "Selective Laser Sintering," Ph.D. Dissertation, Dept. of Mechanical Engineering, Univ. of Texas, Austin, TX, 1988.

[5]Conley, J. G., and Marcus, H. L., "Rapid Prototyping and Solid Freeform Fabrication," *Journal of Manufacturing Science and Engineering*, Vol. 119, No. 4, 1997, pp. 811–816.

[6]Bunnell, D. E., "Fundamentals of Selective Laser Sintering of Metals," Ph.D. Dissertation, Dept. of Mechanical Engineering, Univ. of Texas, Austin, TX, 1995.

[7]Cline, H. E., and Anthony, T. R., "Heat Treating and Melting Material with a Mining Laser or Electron Beam," *Journal of Applied Physics*, Vol. 48, No. 9, 1977, pp. 3895–3900.

[8]Moody, J. E., and Hendel, R. H., "Temperature Profiles Induced by a Scanning CW Laser Beam," *Journal of Applied Physics*, Vol. 53, No. 6, 1982, pp. 4364–4371.

[9]Kant, R., "Laser-Induced Heat of a Multilayered Medium Resting on a Half-Space: Part I: Stationary Source," *Journal of Applied Mechanics*, Vol. 55, No. 1, 1988, pp. 93–97.

[10]Modest, M. F., and Abakians, H., "Heat Conduction in a Moving Semi-Infinite Solid Subjected to Pulsed Laser Irradiation," *Journal of Heat Transfer*, Vol. 108, No. 3, 1986, pp. 597–601.

[11]Kar, A., and Mazumder, J., "Three-Dimensional Transient Thermal Analysis for Laser Chemical Vapor Deposition on Uniformly Moving Finite Slabs," *Journal of Applied Physics*, Vol. 65, No. 8, 1989, pp. 2923–2934.

[12]Pak, J., and Plumb, O. A., "Melting in a Two-Component Packed Bed," *Journal of Heat Transfer*, Vol. 119, No. 3, 1997, pp. 553–559.

[13]Iwamoto, M., Ye, M., Grigoropoulos, C. P., and Greif, R., "Numerical Analysis of Pulsed Laser Heating for the Deformation of Metals," *Numerical Heat Transfer, Part A*, Vol. 34, No. 8, 1998, pp. 791–804.

[14]Han, L., and Liou, F. W., "Numerical Investigation of the Influence of Laser Beam Mode on Melt Pool," *International Journal of Heat and Mass Transfer*, Vol. 47, No. 19-20, 2004, pp. 4385–4402.

[15]Zhang, Y., and Faghri, A., "Melting of a Subcooled Mixed Powder Bed with Constant Heat Flux Heating," *International Journal of Heat and Mass Transfer*, Vol. 42, No. 5, 1999, pp. 775–788.

[16]Zhang, Y., and Faghri, A., "Melting and Resolidification of a Subcooled Mixed Powder Bed with Moving Gaussian Heat Source," *Journal of Heat Transfer*, Vol. 120, No. 4, 1998, pp. 883–891.

[17]Zhang, Y., Faghri, A., Buckley, C. W., and Bergman, T. L., "Three-Dimensional Sintering of Two-Component Metal Powders with Stationary and Moving Laser Beams," *Journal of Heat Transfer*, Vol. 122, No. 1, 2000, pp. 150–158.

[18]Tolochko, N. K., Mozzharov, S. E., Laoui, T., and Froyen, L., "Selective Laser Sintering of Single- and Two-Component Metal Powders," *Rapid Prototyping Journal*, Vol. 9, No. 2, 2003, pp. 68–78.

[19]Tolochko, N. K., Mozzharov, S. E., Sobolenko, N. V., Khlopkov, Y. V., Yadroitsev, I. A., and Mikhailov, V. B., "Main Relationship Governing Laser Sintering of Loose Single-Component Metallic Powders," *Journal of Advanced Materials*, Vol. 2, No. 2, 1995, pp. 151–157.

[20]Tolochko, N. K., Yadroitsev, I. A., Mozzharov, S. E., and Mikhailov, V. B., "Selective Laser Sintering: Some Questions of Physics and Technology," *Proceeding of PM 98 World Congress*, Vol. 5, European Powder Metallurgy Association, Granada, Spain, 1998, pp. 407–412.

[21]Tolochko, N. K., Arshinov, M. K., Gusarov, A. V., Titov, V. I., Laoui, T., and Froyen, L., "Mechanisms of Selective Laser Sintering and Heat Transfer in Ti Powder," *Rapid Prototyping Journal*, Vol. 9, No. 5, 2003, pp. 314–326.

[22]Fischer, P., Romano, V., Weber, H. P., Karapatis, N. P., Boillat, E., and Glardon, R., "Sintering of Commercially Pure Titanium Powder with a Nd:YAG Laser Source," *Acta Materialia*, Vol. 51, No. 6, 2003, pp. 1651–1662.

[23]Eckert, E. R. G., and Drake, R. M., *Analysis of Heat and Mass Transfer*, McGraw–Hill, London, 1972, Chap. 5.

[24]Morgan, R., Sutcliffe, C. J., and O'Neill, W., "Experimental Investigation of Nanosecond Pulsed Nd:YAG Laser Re-melted Pre-placed Powder Beds," *Rapid Prototyping Journal*, Vol. 7, No. 3, 2001, pp. 159–172.

[25]Xiao, B., and Zhang, Y., "Analysis of Melting in a Single-Component Metal Powder Bed Subject to Constant Heat Flux Heating," *Proceedings of 2004 ASME Heat Transfer/Fluid Engineering Summer Conference*, (CD-ROM), American Society of Mechanical Engineers, New York, 2004.

[26]Kaviany, M., *Principles of Heat Transfer in Porous Media*, 2nd ed., Springer-Verlag, New York, 1995.

[27]Cao, Y., and Faghri, A., "A Numerical Analysis of Phase Change Problems Including Natural Convection," *Journal of Heat Transfer*, Vol. 112, No. 3, 1990, pp. 812–816.

[28]Hadley, G. R., "Thermal Conductivity of Packed Metal Powders," *International Journal of Heat and Mass Transfer*, Vol. 29, No. 6, 1986, pp. 909–920.

[29]Patankar, S. V., *Numerical Heat Transfer and Fluid Flow*, McGraw–Hill, New York, 1980.

[30]Carslaw, H. S., and Jaeger, J. C., *Conduction of Heat in Solids*, 2nd ed., Clarendon, Oxford, 1969, pp. 267–271.

[31]Kim, W. H., Fan, H. G., and Na, S. J., "Effect of Various Driving Forces on Heat and Mass Transfer in Arc Welding," *Numerical Heat Transfer*, Part A, Vol. 32, No. 6, 1997, pp. 633–652.

[32]Incropera, F. P., and Dewitt, D. P., *Fundamentals of Heat and Mass Transfer*, 5th ed., Wiley, New York, 2001.